Phase Evolution and Mechanical Behavior of a Novel Ti–6.3Cu–2.2Fe−2.1Al Alloy Processed by Wire-Arc Directed Energy Deposition

MARTIN KLEIN, ELLA STAUFER, DUYAO ZHANG, CHRISTIAN EDTMAIER, JELENA HORKY, MARTIN SCHMITZ-NIEDERAU, DONG QIU, MARK EASTON, and THOMAS KLEIN

Lacking Ti-alloy wires tailored for wire-arc directed energy deposition (waDED) restricts AM-component implementation. Ti–Cu alloys show potential but require additional elements to enhance performance. In this work, waDED-processed Ti–6.3Cu–2.2Fe−2.1Al is characterized. Addition of Cu to Ti achieves a columnar-to-equiaxed transition. The microstructure consists of fine Ti_2Cu precipitates, β matrix, and α plates, with varying morphologies along the deposit's height due to differing thermal histories. The as-built sample exhibits a σ_Y of 1039 MPa but low ductility.

https://doi.org/10.1007/s11661-025-07766-9
© The Author(s) 2025

TODAY'S aviation sector faces challenges, which require investments in its fleet to reduce CO_2 and NO_x emissions.[1] Weight reduction by using lightweight and high-strength materials like Ti alloys is already part of the solution in many airplanes.[2,3] Besides the reduction in emissions through lightweighting with Ti, the environmental impact of the production process is an important consideration in a component's life cycle. Recently, Sword *et al.*[4] reported that using wire-arc directed energy deposition (waDED) instead of conventional forging for a Ti–6Al–4V component reduces carbon emissions by 50 pct, energy consumption by 40 pct, and material waste by 55 pct.[4]

The number of commercial alloy grades available as feedstock wire for waDED is scarce.[5] Despite the perennial progress in additive manufacturing (AM), its slow adoption in aerospace is caused by the second biggest challenge, namely, that conventional alloys were rather developed for casting, forging, or extrusion.[6] AM, however, more analogous to welding, requires alloy compositions adapted to the unique processing conditions to produce defect-free and high-performing components.[6] Conventional Ti alloys yield unfavorable microstructures in AM processes including columnar growth of grains due to the high thermal gradient leading to epitaxial growth, and layer bands resulting from the cyclic reheating of previously deposited layers.[7,8] Efforts to eliminate the anisotropic mechanical properties[7,9] resulting from columnar grain growth have led to in-process solutions like inter-pass rolling,[10] inter-pass machine hammer peening,[11] and other techniques.[12–16] The downside of these though effective techniques is the additional complexity that the setups entail. Thus, other groups have focused on adjusting the alloy composition, which in turn affects the solidification mode. Specifically, alloying elements with a high growth restriction factor have been argued to act as effective refining agents. Recently, also the effects of grain refinement *via* the cyclic transition through solid-state reactions have been analyzed.[17,18] Potential alloying elements able to achieve pronounced grain refinement are, *e.g.*, Fe,[19] W,[20] and Ni,[21] among others. Zhang *et al.*[22] suggested Cu as a potential candidate alloying element in titanium, which was shown in the binary Ti–Cu system using laser-metal deposition with the result of a fully equiaxed

MARTIN KLEIN and THOMAS KLEIN are with the LKR Light Metals Technologies, AIT Austrian Institute of Technology, Lamprechtshausenerstr. 61, 5282 Ranshofen, Austria. Contact e-mail: martin.klein@ait.ac.at ELLA STAUFER is with the Institute of Chemical Technologies and Analytics, TU. Wien, 1060 Vienna, Austria and also with the RHP-Technology GmbH, 2444 Seibersdorf, Austria. DUYAO ZHANG is with the Centre for Additive Manufacturing, School of Engineering, RMIT University, Melbourne 3000, Australia and also with the University of Bath, Bath, BA2 7AY, UK. CHRISTIAN EDTMAIER is with the Institute of Chemical Technologies and Analytics, TU Wien JELENA HORKY is with the RHP-Technology GmbH. MARTIN SCHMITZ-NIEDERAU is with the voestalpine Böher Welding Germany GmbH, 59067 Hamm, Germany. DONG QIU and MARK EASTON are with the Centre for Additive Manufacturing, School of Engineering, RMIT University.
Manuscript submitted December 20, 2024; accepted March 30, 2025.

Published online: 15 April 2025

microstructure.[22] Other works showed that the addition of Cu also accomplished the columnar-to-equiaxed transition (CET) in other than just binary composition and thus consolidated our approach to utilize Cu as the main alloying element to induce the CET.[23–25] Fe and Al influence the phase transformation mechanism and solid-solution strengthening, respectively.[26]

With that motive, the goal of the present work was the microstructural and mechanical characterization of a proposed quaternary alloy composition,[26] which was cast, processed into wire, and used for waDED sample fabrication. The composition of the investigated Ti–6.3Cu–2.2Fe–2.1Al alloy shall have a high constitutional supercooling capacity through high Cu addition. Further, the phase transformation pathway shall be modified by Fe as observed in References 22, 27. To increase the strength, Al is added as a solid-solution hardener. This work intends to examine the microstructural evolution and the tensile strength of this experimental alloy on an AM structure and evaluates its potential application as a future high-performance Ti alloy.

The alloy was cast in 15 kg ingots (GfE Gesellschaft für Elektrometallurgie mbH). Ti and Al concentrations were obtained by means of X-ray fluorescence spectroscopy (XRF), whereas the amounts of Si, Fe, Cu, and C were determined using inductively coupled plasma-optical emission spectroscopy (ICP-OES). The impurity elements O, N, and H were quantified by carrier gas hot extraction analysis (see Table I). Subsequent wire manufacturing was done by preheating a machined billet to 1200 °C for 20 minutes and extruding through a heated 4 mm die. The 4 mm wire was deposited on a 3-mm-thick commercially pure Ti substrate layer by layer using a gas tungsten arc welding system in an open-lid box flushed with argon gas for shielding. The deposit was built in 12 single layers on top of each other, always starting at the same starting point of the deposit with no alternation of the welding torch's traveling direction using gas tungsten arc welding. The resulting deposit had dimensions of 100 × 10 × 35 mm^3 ($L \times W \times H$).

Microstructural imaging was done with a Tescan Mira3 scanning electron microscope (SEM) in a four-quadrant-backscattered electron (BSE) and secondary electron (SE) mode, while macrographs were captured with an Olympus BX53M light microscope. Metallographic preparation consisted of embedding in electrically conductive resin, grinding with 320 P to 2400 P SiC paper, and polishing for 5 minutes using an oxide polishing suspension (OP-S, particle size 0.04 μm) before final polishing for 5 minutes with a mixture of 90 vol pct OP-S and 10 vol pct hydrogen peroxide (30 pct). Preparation for optical light microscopy (OLM) included etching with buffered oxide etchant (BOE) 10:1, which was diluted with distilled water to 40 pct BOE as proposed in Reference 28. The etched samples were imaged using a color polarizer (Olympus U-GAN gout analyzer). EBSD maps were captured on a JOEL 7200F SEM at 20 kV with a step size of 0.5 μm. Parent grains (prior-β) were reconstructed using the Aztec Crystal (v3.1) software assuming a Burgers orientation relationship (BOR). Focused ion beam (gallium) milling on a FEI Scios SEM was used to prepare the samples for energy dispersion spectroscopy (EDS) analysis, and the EDS line scans were performed at 200 kV on a JEOL2100 transmission electron microscope (TEM). X-ray diffraction (XRD) was performed with an X'pert^3 powder diffractometer (Malvern Panalytical) in Bragg–Brentano geometry with X'Celerator detectors. CuK_α radiation was used, and the scans were conducted with steps of 0.02 deg. Phase analysis was performed with the X'pert HighScore software.

The flat tensile testing sample was milled from the deposit with a geometry according to DIN 50125-E 2 × 6 × 20 mm^3 ($T \times W \times L$). Testing was performed in the as-built condition at room temperature using a Zwick Z100 BZ 100/SN3A with an extensometer according to the ÖNORM-EN-ISO 6892-1B with 10 N/mm^{2}s until reaching σ_Y and a constant strain rate of 0.0067 s^{-1} beyond. For microhardness measurements, an EMCO-TEST DuraScan 70G5 was used according to the DIN-EN-ISO 6507—Vickers hardness test.

The grain structure was analyzed by OLM (Figure 1) to analyze the susceptibility of the experimental alloy to columnar grain growth. Identifying the parent grain structure has been shown to be difficult in binary Ti–Cu alloys, due to the potential superposition of solidification microstructure and solid-state transformation microstructure.[29] In the investigated alloy, the latter phenomenon is, however, negligible, since no coupled growth of α phase and Ti_2Cu phase (pearlite) was observed (see subsequent SEM analysis). Thus, no colony structure is formed that could interfere with the solidification microstructure. Epitaxial nucleation together with preferential growth along the thermal gradient can result in a columnar grain structure.[30] The microstructure in the first layer deposited on the substrate (Figure 1) shows mildly elongated grains pointing toward the top of the deposit with a slight inclination angle toward the surface. However, the next layer exhibits a shift from mildly columnar to also large, but mainly equiaxed grains.

Figure 2(a) shows the grain structure from the top of the build to several layers below with the layer boundaries indicated. Corresponding images in higher magnification are shown in Figures 2(c) and (d). No changes in the primary grain structure are encountered through repetitive reheating of layers and the corresponding thermal cycling through the solid-state β-to-α phase transformation. The EBSD image [Figure 2(b)], corresponding to Figure 2(d), of reconstructed β grains in Y–Z plane evidences equiaxed grains in the upper region of the build. Grain boundaries show little curvatures and triple junctions appear close to ideal angles of 120 deg suggesting that the grain structure is close to equilibrium conditions. Comparing the Y–Z plane in Figure 2(d) with the X–Y plane in Figure 1 suggests that grains are finer in X–Y compared to Y–Z. This most likely originates from the thermal gradient prevailing during AM conditions. In comparison, the grains in X–Y plane (see Figure 1) are finer and more equiaxed. It is noted that for the reconstruction of the β parent grain structure, the BOR was assumed, which is likely present

Table I. Actual Elemental Composition of Alloy Obtained and Provided by GfE mbH

Element	Ti	Cu	Fe	Al	Si	C	H	N	O
Concentration [Wt Pct]	89.0	6.3	2.2	2.1	0.001	0.006	0.001	0.005	0.030

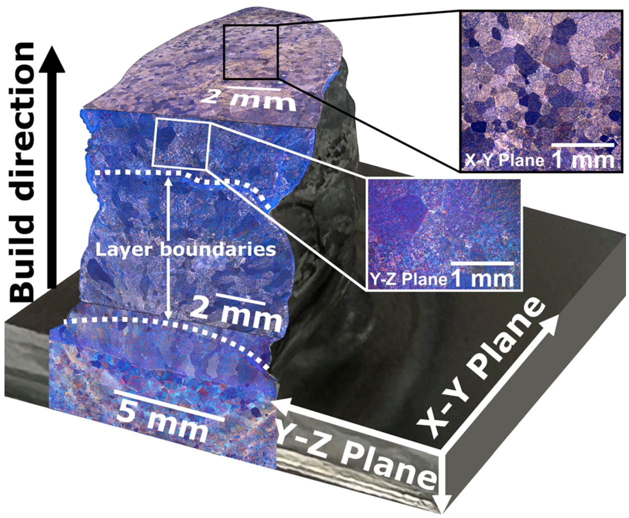

Fig. 1—OLM image showing the etched microstructure of the Ti–6.3Cu–2.2Fe–2.1Al deposit. All observable layer boundaries in this image are marked.

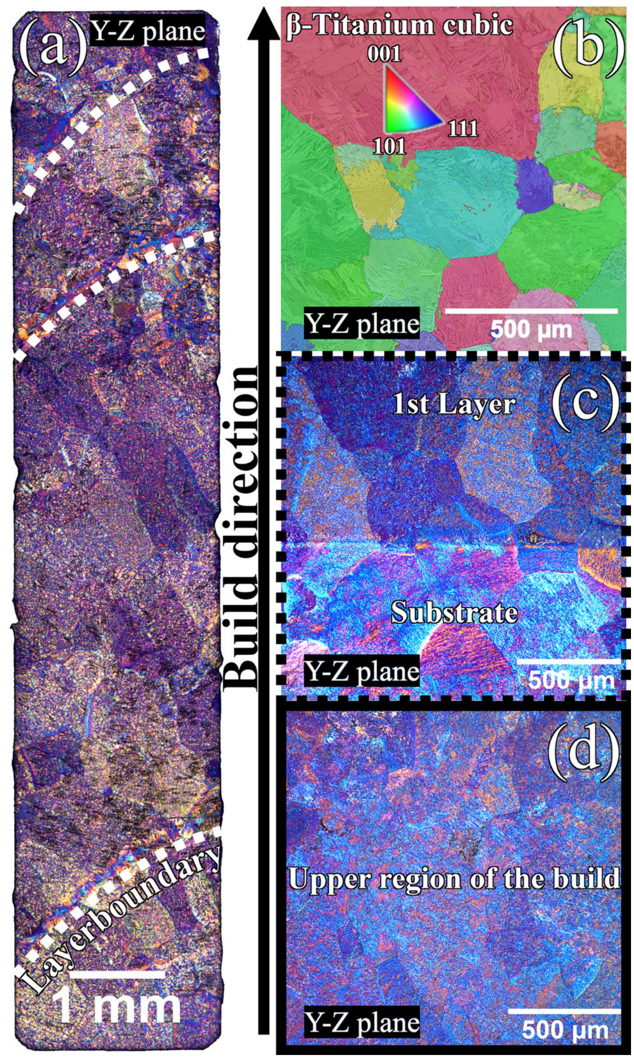

Fig. 2—(*a*) OLM image showing the cross section (Y–Z plane) of the tensile sample, which was extracted out of the last layers of the deposit, as shown in Fig. 6(b); Note that the cross section contains three layer boundaries (marked by white dashed lines); (*b*) EBSD map of the microstructure in build direction; (*c*) higher magnified OLM image; (*d*) OLM image from the upper region of the build.

in martensitic microstructures (see Figure 3 and Reference 29). Saville *et al.*[17] have recently suggested that thermal cycling in the solid-state phase transformation regime of Ti–Cu alloys causes refinement similarly as it is the case in well-known steel alloys. However, the present work implies that a refined primary structure in comparison to Ti–6Al–4V processed similarly (see *e.g.*, Neves *et al.*[31]) is already present upon initial solidification.

Figure 3 depicts SEM micrographs taken in X–Y and Y–Z planes with their respective microhardness values. The morphology of the α plates (dark contrasted features) in Figure 3 shows pronounced differences regarding location within the deposit. α plates close to the substrate [Figure 3(a)] grew larger to a lenticular shape (average ~ 2.85 μm^2), whereas these close to the top layer [Figure 3(b)] exhibit a very thin (average ~ 1.0 μm^2) and closely packed lath structure. Driven by the repeated reheating of already deposited layers, α plates coarsen due to a prolonged time for β-to-α transformation and growth at the expense of dissolving smaller α plates. The gradual coarsening of α-plates toward the bottom is most likely also responsible for the measurable difference in microhardness of 340 $HV_{0.1}$ at the bottom and 360 $HV_{0.1}$ at the top. The smaller spacing between the lamellar α plates in Figure 3(b) compared to Figure 3(a) means a larger α/β interface area, and thus a higher density of barriers for dislocation movement according to the Hall–Petch relationship.[32]

At the α/β interface found between α plates and β matrix, a third phase is visible, especially in Figure 3(a) (white contrasted features). In the literature,[27,33–35] the intermetallic Ti_2Cu phase is typically observed in alloys based on Ti–Cu. The BSE images show that it grows nearly exclusively at α/β interfaces, due to its evolution by the decomposition of $\beta \rightarrow \alpha + Ti_2Cu$.[36] However, the cooperative eutectoid reaction is suppressed by the presence of Fe.[26] Upon reheating into the β-phase region it is argued that the β phase inherits the orientation from the retained β phase acting as nucleus enabling an effect that is well documented in steels and

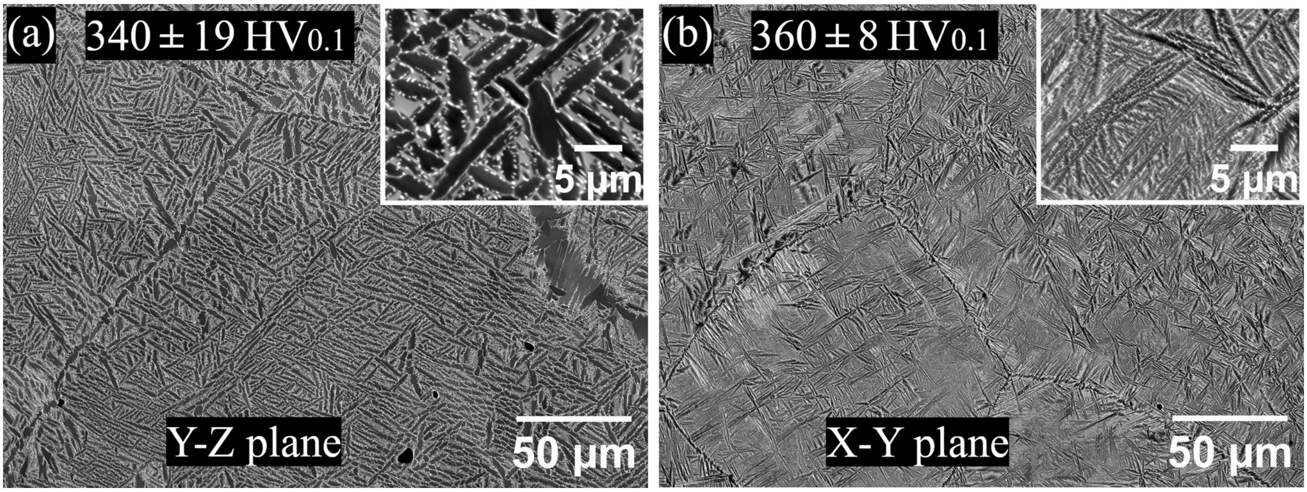

Fig. 3—BSE images showing the microstructure of the deposit in the (*a*) Y–Z plane located in the first layer and in the (*b*) X–Y plane located in the third layer of the build (for orientation see Fig. 1) with respective magnifications.

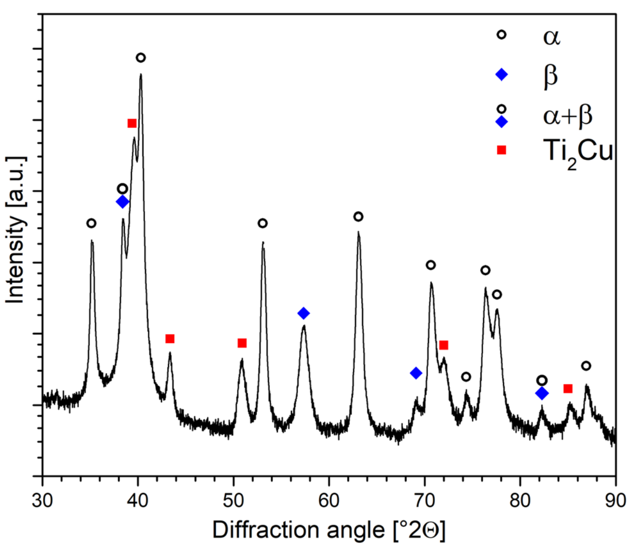

Fig. 4—XRD analysis of the experimental Ti–6.3Cu–2.2Fe–2.1Al alloy.

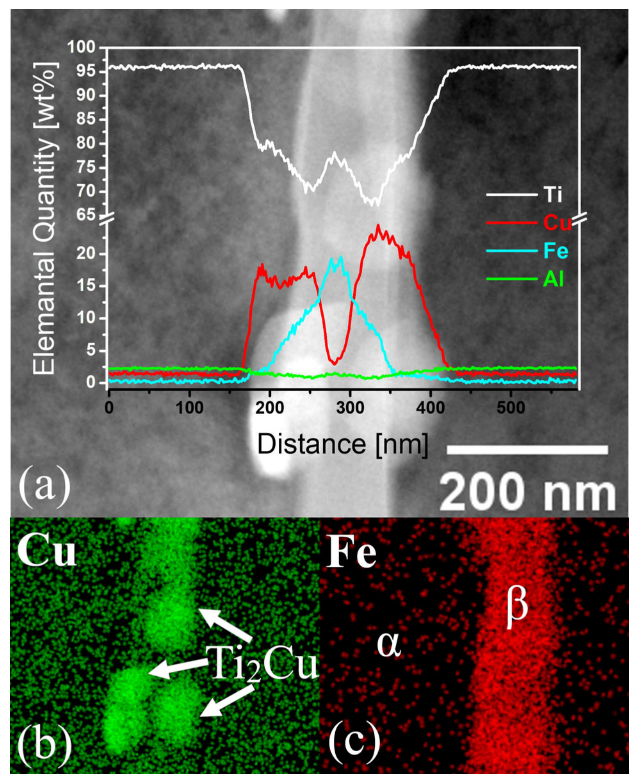

Fig. 5—(*a*) TEM image with an overlayed EDS line scan recorded at the same position as the *x*-axis. (*b*) and (*c*) show the respective element distribution maps for Cu and Fe in the shown TEM image.

referred to as austenite memory mechanism.[37] Therefore, the effects of thermal cycling shown by Saville *et al*.[17,18] do not prevail in the present alloy.

Additionally, the α/β interface corresponds to the most effective nucleation site for the Ti_2Cu precipitates in the investigated $\alpha + \beta$-alloy, similar to the α/α' (martensite) boundaries in binary Ti-xCu α alloys.[38] The further progressed decomposition of β in the layers closer to the substrate, as explained before, also results in the growth of Ti_2Cu precipitates to a larger size, and therefore better visibility in Figures 3(a) than in (b).

Individual primary β grains are distinguishable by the preferential formation of α phase at their grain boundaries.[39] This morphological feature is typically undesirable as premature failure can occur due to strain localization and subsequent crack formation.[40] The grain boundary α seems to have grown mostly in a discontinuous manner.

XRD was conducted to clarify the nature of phases, present in the Ti–6.3–2.2Fe–2.1Al alloy. Figure 4 shows texture wherefore a quantitative statement about phase fractions is restricted. The comparably small β peaks suggest that qualitatively α is the dominant phase in relation to the amount of β. The peak at 57.3 deg is clearly indexed as β phase. All other peaks can be clearly indexed using the Ti_2Cu structure. Slight peak broadening can be observed, which corresponds to the nm-scaled size distribution of this phase.

Figure 5 presents a TEM bright-field image with an overlayed EDS line scan, where the x-axis represents the distance along the scanned line. The film-like phase with bright gray contrast represents the β phase, whereby the brighter contrast phase is the Ti_2Cu intermetallic phase as the preferred segregation of Fe to the β phase and Cu to the Ti_2Cu phase has been shown recently.[26] The surrounding dark contrasted feature corresponds to the α phase. A clear identification of individual Ti_2Cu particles can be made based on the EDS maps shown in Figures 5(b) and (c) with pronounced Cu enrichment in these precipitates. Further proof of their presence besides the decrease in Fe and Al is also the lower concentration of Ti, as its elemental ratio in Ti_2Cu is lower than in the α or β phases [see Figure 5(a)]. Cu is only found at trace amounts within the β phase as it mostly redistributed into the intermetallic phase. Both Fe and Al are absent in the Ti_2Cu precipitate as they preferentially partition into β and α phases, respectively. Fe is among the strongest β-stabilizing elements obviously favoring the β-phase solid solution. Cu can also be observed in β phase to a lower extent. The only included α-stabilizer Al is found to primarily partition into α. A slightly higher Al concentration between the Ti_2Cu particles is visible.

In Figure 6(a), the stress–strain curve of the single tensile sample is shown. More samples were not obtainable due to limited amount of wire available. Testing in the X–Y plane was specifically chosen to measure the potentially lowest mechanical properties in the case of directional grain growth. In (quasi-)static loading scenarios, grain boundaries in many Ti alloys are preferred crack initiation points due to the pile up of dislocations. Thus, testing either along the elongated grain (along Y–Z) or in X–Y and there schematically pulling apart the grains at the boundaries, results in lower mechanical properties when testing in X–Y plane.

The alloy reached an ultimate tensile strength (σ_{UTS}) of 1089 MPa, a yield strength (σ_Y) of 1039 MPa, and a total elongation (A) of 1.41 pct. Compared with the widely used Ti–6Al–4V, which reaches σ_Y of 908 to 1105 MPa, σ_{UTS} of 984 to 1163 MPa, and an elongation A of 2.4 to 8.2 pct in the as-built conditions,[41–46] the investigated Ti–6.3Cu–2.2Fe–2.1Al alloy features an equally high strength but lacks sufficient ductility. Similar ductility values were recently reported by Klein *et al.*[47] using the same alloy in cast and cast + extruded material conditions suggesting that the low fracture strain is a material property rather than a result of a processing-induced defects as any potential casting porosity would have been closed by the high deformation degrees encountered during extrusion.

The fracture surface in Figure 6(c) reveals an intragranular crack propagation as no individual protruding grains are visible. The edges at the upper corners of the sample show a particularly smooth surface, which might indicate a notch effect. Whether the edges acted as fracture initiation points or represent the residual fracture face is unclear. Most likely the fracture initiated in the area marked with the red circle in Figure 6(c) as optically the linear topological features are orientated like rays toward this point. It is further evident that the tensile sample exhibits some porosity throughout the bulk material with maximum pore diameters of around 50 μm. However, the potential fracture initiation area

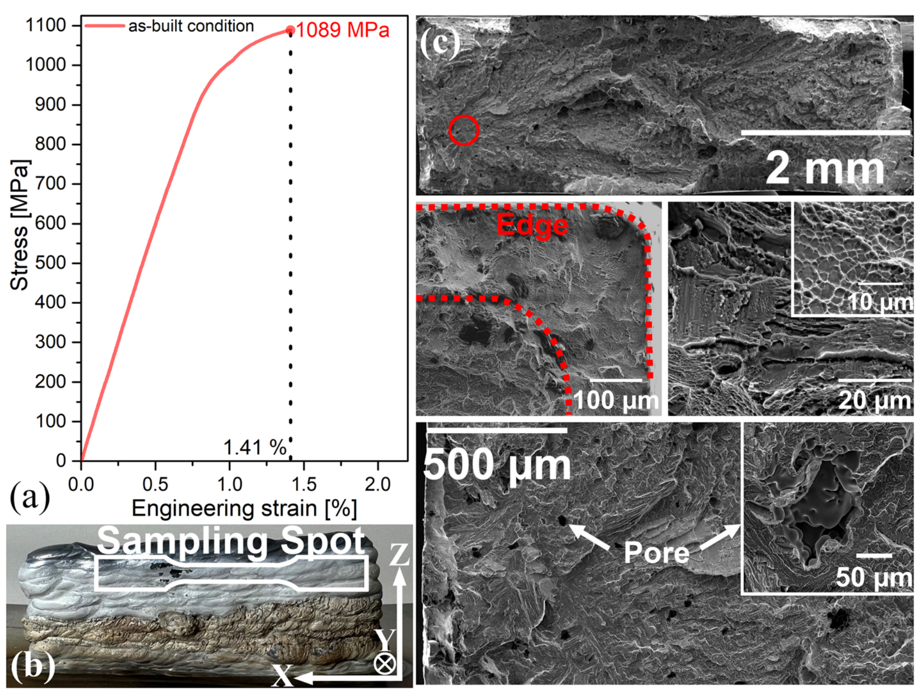

Fig. 6—(*a*) Tensile test result of the flat tensile sample in the as-built condition, extracted from the deposit (*b*). (*c*) Secondary electron images of the whole fracture surface after tensile testing.

does not show that the initial crack developed at one of these pores. Other defects as cracks from hot tearing, delamination, or lack of fusion were not observed.

On cooling below the eutectoid temperature of Ti–6.3Cu–2.2Fe–2.1Al, intermetallic Ti_2Cu phase is formed. Due to Cu enrichment in the vicinity of the moving α/β phase boundary as well as favored heterogeneous nucleation, these particles nucleate solely along these interfaces. The repetitive reheating of the layers during each subsequent pass provides the necessary alloying element redistribution required for diffusive growth. The final microstructure comprises α, β, and Ti_2Cu phases, with the earlier being the dominant phase and the latter being the minority phase. The mechanical properties reflect the fine microstructural features in the form of high strength but low ductility and small work hardening capacity. Fracture analysis shows intragranular failure implying that the grain boundary α [48] does not represent the site for crack propagation. However, it must be noted that the presented results do not resolve enough evidence to prove the full discontinuity of the grain boundary α.

In summary, the experimental alloy composition Ti–6.3Cu–2.2Fe–2.1Al demonstrates that the concept for refinement of the primary grain structure can be exploited, while simultaneously obtaining a high mechanical strength. Although a columnar-to-equiaxed transition was observed in the material, the grain structure remained relatively coarse. A local difference is observed in the growth of α plates to larger lenticular shapes in the former layers, while small laths dominate in upper layers. The hardness also varies alongside these microstructural differences. The deficiency in ductility can potentially be optimized and balanced properties may be obtained by further optimizing alloy composition and by applying subsequent heat treatments, on which the focus should be laid in future research. Further trials with this material on waDED equipment should be done to gather more insights into the effects of processing on the mechanical properties.

ACKNOWLEDGMENTS

This work was supported by the Austrian Federal Ministry for Climate Action, Environment, Energy, Mobility, Innovation and Technology (BMK) within the aeronautics funding program "Take Off," project "highTi—Novel high-strength titanium alloys for aeronautic applications" administered by FFG [grant number 886889] and the Australian Research Council (Grant Number DE210101503, DP220101501].

FUNDING

Open access funding provided by AIT Austrian Institute of Technology GmbH.

CONFLICT OF INTEREST

On behalf of all authors, the corresponding author states that there is no conflict of interest.

OPEN ACCESS

This article is licensed under a Creative Commons Attribution 4.0 International License, which permits use, sharing, adaptation, distribution and reproduction in any medium or format, as long as you give appropriate credit to the original author(s) and the source, provide a link to the Creative Commons licence, and indicate if changes were made. The images or other third party material in this article are included in the article's Creative Commons licence, unless indicated otherwise in a credit line to the material. If material is not included in the article's Creative Commons licence and your intended use is not permitted by statutory regulation or exceeds the permitted use, you will need to obtain permission directly from the copyright holder. To view a copy of this licence, visit http://creativecommons.org/licenses/by/4.0/.

REFERENCES

1. Publications Office of the European Union: *European Commission*, 2012, https://doi.org/10.2777/15458.
2. P. Nyamekye, S. Rahimpour Golroudbary, H. Piili, P. Luukka, and A. Kraslawski: *Adv. Ind. Manuf. Eng.*, 2023, vol. 6, p. 100112.
3. L. Zhu, N. Li, and P.R.N. Childs: *Propul. Power Res.*, 2018, vol. 7, pp. 103–19. https://doi.org/10.1016/J.JPPR.2018.04.001.
4. J.I. Sword, A. Galloway, and A. Toumpis: *Sustain. Mater. Technol.*, 2023, vol. 36, p. e00600. https://doi.org/10.1016/J.SUSMAT.2023.E00600.
5. H. Pant, A. Arora, G.S. Gopakumar, U. Chadha, A. Saeidi, and A.E. Patterson: *Int. J. Adv. Manuf. Technol.*, 2023, vol. 127, pp. 4995–5011. https://doi.org/10.1007/S00170-023-11623-7.
6. B. Bihlman: Additive Manufacturing and Supply Chain Readiness for Aerospace Production. International Titanium Association, 2024. https://issuu.com/titaniumtoday/docs/titaniumtoday_042224. Accessed 01 September 2024.
7. D. Chakraborty, T. Tirumala, S. Chitral, B.N. Sahoo, D.V. Kiran, and P.A. Kumar: *J. Mater. Eng. Perform.*, 2022, vol. 31, pp. 6149–82. https://doi.org/10.1007/S11665-022-07128-1.
8. A. Ho, H. Zhao, J.W. Fellowes, F. Martina, A.E. Davis, and P.B. Prangnell: *Acta Mater.*, 2019, vol. 166, pp. 306–23. https://doi.org/10.1016/J.ACTAMAT.2018.12.038.
9. E. Brandl, B. Baufeld, C. Leyens, and R. Gault: *Phys. Procedia*, 2010, vol. 5, pp. 595–606. https://doi.org/10.1016/J.PHPRO.2010.08.087.
10. F. Martina, P.A. Colegrove, S.W. Williams, and J. Meyer: *Metall. Mater. Trans. A*, 2015, vol. 46, pp. 6103–18. https://doi.org/10.1007/S11661-015-3172-1.
11. L. Neto, S. Williams, J. Ding, J. Hönnige, and F. Martina: in *Lecture Notes in Mechanical Engineering*. S. Itoh and S. Shukla, eds., Springer, Singapore, 2020, pp. 121–32. https://doi.org/10.1007/978-981-15-0054-1_13.
12. Z. Li, C. Liu, T. Xu, L. Ji, D. Wang, J. Lu, S. Ma, and H. Fan: *Mater. Sci. Eng. A*, 2019, vol. 742, pp. 287–94. https://doi.org/10.1016/J.MSEA.2018.11.022.
13. Y. Yang, X. Jin, C. Liu, M. Xiao, J. Lu, H. Fan, and S. Ma: *Metals (Basel)*, 2018, vol. 8, p. 934. https://doi.org/10.3390/MET8110934.
14. J. Gou, Z. Wang, S. Hu, J. Shen, Y. Tian, G. Zhao, and Y. Chen: *J. Manuf. Process.*, 2020, vol. 54, pp. 148–57. https://doi.org/10.1016/J.JMAPRO.2020.03.010.
15. D. Ding, B. Wu, Z. Pan, Z. Qiu, and H. Li: *Mater. Manuf. Process.*, 2020, vol. 35, pp. 845–51. https://doi.org/10.1080/10426914.2020.1732414.
16. S. Sundaresan and G.D. Janaki Ram: *Sci. Technol. Weld. Join.*, 1999, vol. 4, pp. 151–60. https://doi.org/10.1179/136217199101537699.
17. A.I. Saville, O.W. Hesmondhalgh, N.A. Compton, G.A. Thompson, M. Sanders, J. Klemm-Toole, K.D. Clarke, H.L. Fraser, M.J.

Kaufman, A. Karma, and A.J. Clarke: *Addit. Manuf.*, 2023, vol. 75, p. 103747. https://doi.org/10.1016/J.ADDMA.2023.103747.
18. A.I. Saville, A. Eres-Castellanos, A.B. Kustas, L. Van Bastian, D.F. Susan, D.E. Cillessen, S.C. Vogel, N.A. Compton, K.D. Clarke, A. Karma, and A.J. Clarke: *Mater. Des.*, 2024, vol. 248, p. 113440. https://doi.org/10.1016/J.MATDES.2024.113440.
19. M. Simonelli, D.G. McCartney, P. Barriobero-Vila, N.T. Aboulkhair, Y.Y. Tse, A. Clare, and R. Hague: *Metall. Mater. Trans. A*, 2020, vol. 51, pp. 2444–59. https://doi.org/10.1007/s11661-020-05692-6.
20. M.Y. Mendoza, P. Samimi, D.A. Brice, B.W. Martin, M.R. Rolchigo, R. LeSar, and P.C. Collins: *Metall. Mater. Trans. A*, 2017, vol. 48, pp. 3594–3605. https://doi.org/10.1007/s11661-017-4117-7.
21. B.A. Welk, N. Taylor, Z. Kloenne, K.J. Chaput, S. Fox, and H.L. Fraser: *Metall. Mater. Trans. A*, 2021, vol. 52, pp. 5367–80. https://doi.org/10.1007/S11661-021-06475-3.
22. D. Zhang, D. Qiu, M.A. Gibson, Y. Zheng, H.L. Fraser, D.H. StJohn, and M.A. Easton: *Nature*, 2019, vol. 576, pp. 91–95. https://doi.org/10.1038/s41586-019-1783-1.
23. X. Li, Z. Yao, X. Tao, M. Yao, and S. Zhang: *Vacuum*, 2021, vol. 194, p. 110638. https://doi.org/10.1016/j.vacuum.2021.110638.
24. A.P. Zykova, A.V. Nikolaeva, A.V. Vorontsov, A.V. Chumaevskii, S.Y. Nikonov, E.N. Moskvichev, D.A. Gurianov, N.L. Savchenko, E.A. Kolubaev, and S.Y. Tarasov: *Phys. Mesomech.*, 2023, vol. 26, pp. 107–25. https://doi.org/10.1134/S1029959923020017.
25. A.M. Vilardell, I. Yadroitsev, I. Yadroitsava, M. Albu, N. Takata, M. Kobashi, P. Krakhmalev, D. Kouprianoff, G. Kothleitner, and A. du Plessis: *Addit. Manuf.*, 2020, vol. 36, p. 101436. https://doi.org/10.1016/j.addma.2020.101436.
26. T. Klein, D. Zhang, E. Staufer, T. Boll, C. Schneider-Broeskamp, C. Edtmaier, M. Schmitz-Niederau, J. Horky, D. Qiu, and M. Easton: *J. Mater. Res. Technol.*, 2023, vol. 27, pp. 4978–85. https://doi.org/10.1016/J.JMRT.2023.11.014.
27. Y. Xu, J. Jiang, Z. Yang, Q. Zhao, Y. Chen, and Y. Zhao: *Materials*, 2020, vol. 13, p. 3411. https://doi.org/10.3390/MA13153411.
28. J. Dumbre, Z. Tong, D. Dong, D. Qiu, and M. Easton: *Metallogr. Microstruct. Anal.*, 2024, https://doi.org/10.1007/S13632-024-01094-X.
29. A.I. Saville and A.J. Clarke: *Mater Charact*, 2023, vol. 196, p. 112569. https://doi.org/10.1016/J.MATCHAR.2022.112569.
30. V.P. Narayana Samy, M. Schäfle, F. Brasche, U. Krupp, and C. Haase: *Addit. Manuf.*, 2023, vol. 73, p. 103702. https://doi.org/10.1016/J.ADDMA.2023.103702.
31. J.L. Neves, N. Papenberg, D. Kiener, and T. Klein: *JOM*, 2024, https://doi.org/10.1007/S11837-024-06956-X/FIGURES/8.
32. C. Leyens and M. Peters: *Titanium and Titanium Alloys: Fundamentals and Applications*, 1st ed. Wiley-VCH, Weinheim, 2003, pp. 112–13.
33. P. Mukhopadhyay, V. Singh, A. Bhattacharjee, and A.K. Gogia: *Mater. Today Proc.*, 2015, vol. 2, pp. 3580–85. https://doi.org/10.1016/J.MATPR.2015.07.099.
34. Z. Ma, L. Ren, R. Liu, K. Yang, Y. Zhang, Z. Liao, W. Liu, M. Qi, and R.D.K. Misra: *J. Mater. Sci. Technol.*, 2015, vol. 31, pp. 723–32. https://doi.org/10.1016/J.JMST.2015.04.002.
35. K. Dyal Ukabhai, U.A. Curle, N.D.E. Masia, M. Smit, I.A. Mwamba, S. Norgren, C. Öhman-Mägi, N.G. Hashe, and L.A. Cornish: *J. Phase Equilib. Diffus.*, 2022, vol. 43, pp. 332–44. https://doi.org/10.1007/S11669-022-00964-7.
36. T.A. Bhaskaran, R.V. Krishnan, and K. Srinivasa Raghavan: *Scripta Metall.*, 1985, vol. 19, pp. 319–22. https://doi.org/10.1016/0036-9748(85)90322-9.
37. D. Brandl, M. Lukas, M. Stockinger, S. Ploberger, and G. Ressel: *Mater. Des.*, 2019, vol. 176, p. 107841. https://doi.org/10.1016/J.MATDES.2019.107841.
38. J.C. Williams, R. Taggart, and D.H. Polonis: *Metall. Trans.*, 1971, vol. 2, pp. 1139–48. https://doi.org/10.1007/BF02664246.
39. G. Lütjering and J.C. Williams: *Titanium: Engineering Materials and Processes*, 2nd ed. Springer, Berlin, 2007, p. 32.
40. Z. Yan, K. Wang, Y. Zhou, X. Zhu, R. Xin, and Q. Liu: *Scripta Mater.*, 2018, vol. 156, pp. 110–14. https://doi.org/10.1016/J.SCRIPTAMAT.2018.07.023.
41. G.P. Dinda, L. Song, and J. Mazumder: *Metall. Mater. Trans. A*, 2008, vol. 39, pp. 2914–22. https://doi.org/10.1007/S11661-008-9634-Y.
42. Y. Zhai, D.A. Lados, E.J. Brown, and G.N. Vigilante: *Int. J. Fatigue*, 2016, vol. 93, pp. 51–63. https://doi.org/10.1016/J.IJFATIGUE.2016.08.009.
43. J. Alcisto, A. Enriquez, H. Garcia, S. Hinkson, T. Steelman, E. Silverman, P. Valdovino, H. Gigerenzer, J. Foyos, J. Ogren, J. Dorey, K. Karg, T. McDonald, and O.S. Es-Said: *J. Mater. Eng. Perform.*, 2011, vol. 20, pp. 203–12. https://doi.org/10.1007/S11665-010-9670-9.
44. A.J. Sterling, B. Torries, N. Shamsaei, S.M. Thompson, and D.W. Seely: *Mater. Sci. Eng. A*, 2016, vol. 655, pp. 100–12. https://doi.org/10.1016/J.MSEA.2015.12.026.
45. E. Farabi, T. Klein, M. Schnall, and S. Primig: *Addit. Manuf.*, 2023, vol. 71, p. 103592. https://doi.org/10.1016/J.ADDMA.2023.103592.
46. L. Vazquez, M.N. Rodriguez, I. Rodriguez, and P. Alvarez: *Metals (Basel)*, 2021, vol. 11, p. 1161. https://doi.org/10.3390/MET11081161.
47. M. Klein, E. Staufer, C. Edtmaier, J. Horky, M. Schmitz-Niederau, D. Zhang, D. Qiu, M. Easton, and T. Klein: *Adv. Eng. Mater.*, 2024, vol. 26, p. 2400534. https://doi.org/10.1002/ADEM.202400534.
48. J.W. Foltz, B. Welk, P.C. Collins, H.L. Fraser, and J.C. Williams: *Metall. Mater. Trans. A*, 2011, vol. 42, pp. 645–50. https://doi.org/10.1007/S11661-010-0322-3.

Publisher's Note Springer Nature remains neutral with regard to jurisdictional claims in published maps and institutional affiliations.